

Pinhole camera model with refraction correction for tomographic PIV inside cylinders

Gerardo Paolillo^{1*}, Tommaso Astarita¹

¹Università degli Studi di Napoli “Federico II”, Dipartimento di Ingegneria Industriale, Napoli, Italia

*gerardo.paolillo@unina.it

Abstract

The present work addresses the development of a camera calibration model, based on the pinhole approximation and Snell’s law of refraction, for tomographic particle image velocimetry measurements inside transparent cylinders. Such a model adds to the pinhole-camera model parameters a relatively small number of parameters, which have an unambiguous geometrical or physical meaning. A calibration procedure for the innovative camera model is also outlined. Finally, the innovative model is comparatively assessed against the classical pinhole camera model and different polynomial-based models by using experimental data from an investigation of Rayleigh-Bénard convection.

1 Introduction

In last years, Tomographic Particle Image Velocimetry (T-PIV) has proved as a powerful tool for investigation of different types of flows (Scarano, 2012). While its essential advantage consists in the 3D reconstruction of the fluid velocity field in a non-intrusive way, recognized limitations are the requirement for high light power, the relatively small achievable spatial resolution and the expensive computational burden associated with the post-processing. Additional issues may result from optical distortions which can compromise the accuracy of measurements. This is common to flow fields characterized by strong density gradients, such as high-speed currents and thermal flows, but also to incompressible internal flows occurring in complex confined geometries, which are necessarily imaged through the curved transparent sidewalls. In both cases, the optical distortions impact on the calibration of the camera system, posing essentially two difficulties: the selection of an appropriate camera model, which accounts for the optical distortions, and the correct determination of the model parameters.

In this work, such problems are addressed in a specific case, namely the investigation of a fluid motion inside a transparent cylinder. A novel camera model relying on the physical laws of perspective and refraction is introduced and experimentally assessed. From an application standpoint, this is relevant to a wide range of situations, involving both research on fundamental turbulent flows, like pipe flow (Marusic et al., 2010), Rayleigh-Bénard convection (Ahlers et al., 2009) and Taylor-Couette flow (Tokgoz et al., 2012), and technology, including in-cylinder flows of internal-combustion and diesel engines (Agarwal et al., 2017), precessing jets (Cafiero et al., 2014), etc. On the purely technical side, despite the simplicity of the geometry, the present analysis shows the flaws and limitations of the camera calibration models commonly used in the literature for the purpose of determining the mapping function from positions in the interior of a curved (transparent) body to their projections on the camera sensor.

In T-PIV applications, the mostly adopted camera models are the Tsai-Heikkila pinhole camera model (Tsai, 1987; Heikkila and Silven, 1997) and the polynomial models (e.g., Soloff et al., 1997). Based on perspective laws, the pinhole camera model treats the Lines Of Sight (LOSs) as straight lines, whereas lens non-linearity is included via second-order spherical distortion terms. Despite its simplicity, this model does not include the effects of distortions along the LOSs (except the localized lens distortions). Optical misalignment, thermal deformation and refraction by optical windows or fluid interfaces are some of the elements not involved in the model and could lead to high calibration errors. When one or several of the above effects have some importance, polynomial mapping functions generally offer higher performance. Polynomial models generally lead to significantly lower calibration errors due to the redundant number of parameters involved, which allows to compensate for imperfections in the imaging system better than the pinhole camera models, which, conversely, feature corrections based only on a limited number of coefficients

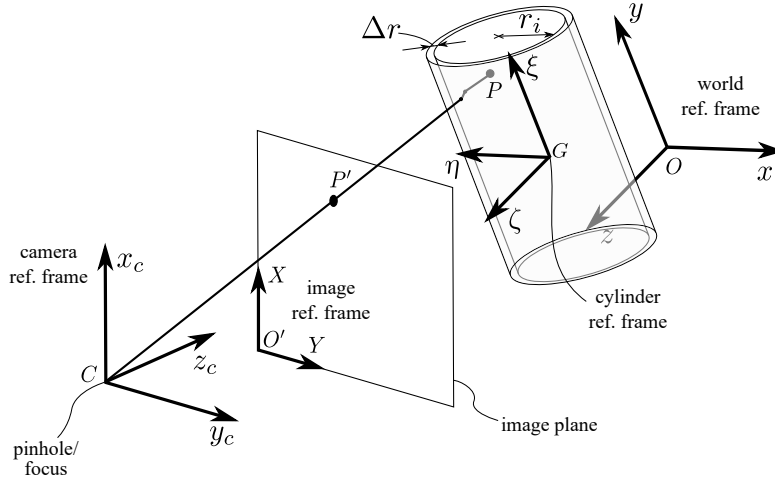


Figure 1: Perspective projection model with the inclusion of a cylindrical optical element.

(typically four or six). On the other side, the same redundancy of the polynomial models may result in large projection errors when computing the polynomial function in locations in between the control points or outside of this grid, while the pinhole camera models obviate such an issue by relying on the physical laws of perspective.

The camera calibration model introduced in this work retains the advantages of the classical pinhole camera models by introducing a correction based on the physical laws of refraction. In such a way, the twofold refraction of the lines-of-sight at the external and the internal surface of the cylinder sidewall can be accurately represented by a small number of parameters. In the following, first the principle of the model is introduced, then a calibration procedure is outlined. Finally, the novel camera model is comparatively assessed against the classical pinhole camera model and the polynomial functions, proving its superior performance, by using experimental data from an investigation of Rayleigh-Benard convection in a cylindrical sample.

2 Proposed camera model

The basic idea of the proposed camera model is to integrate the pinhole camera model with Snell's law in order to accurately represent the cylindrical deformation. The corresponding imaging model is shown in Fig. 1, where it is possible to identify four different reference frames: the world reference frame $Oxyz$, the image reference frame $O'XY$, the camera reference frame $Cx_cy_cz_c$ and the reference frame $G\xi\eta\zeta$ attached to the cylinder. The ξ -axis is chosen to be coincident with the cylinder axis, whereas, due to the axisymmetry of the cylindrical element, the η - and ζ - axes can be chosen arbitrarily. Moreover, for the discussion to follow, it is assumed that the cylinder extends infinitely along the ξ -direction, in such a way that also the location of the origin G can be chosen in an arbitrary way along the cylinder axis.

With the above assumptions, the location and orientation of the cylinder with respect to the world reference frame are identified by only four parameters, namely two translations and two Euler angles. The transformation from the cylinder reference frame to the world reference frame is therefore given by:

$$\begin{bmatrix} \xi \\ \eta \\ \zeta \end{bmatrix} = \begin{bmatrix} \cos(\alpha_c) & \sin(\alpha_c) & 0 \\ -\sin(\alpha_c) & \cos(\alpha_c) & 0 \\ 0 & 0 & 1 \end{bmatrix} \begin{bmatrix} \cos(\beta_c) & 0 & \sin(\beta_c) \\ 0 & 1 & 0 \\ -\sin(\beta_c) & 0 & \cos(\beta_c) \end{bmatrix} \begin{bmatrix} x \\ y \\ z \end{bmatrix} + \begin{bmatrix} 0 \\ \eta_0 \\ \zeta_0 \end{bmatrix} \quad (1)$$

where β_c and α_c are the Euler angles corresponding to rotations about the η - and ζ -axes respectively (3-2-1 sequence), while η_0 and ζ_0 are translations along the same directions. Due to the axisymmetry and the infinite height of the cylinder, the rotation γ_c about the ξ -axis and the translation ξ_0 can be chosen arbitrarily. Equation (1) corresponds to the choice $\gamma_c = 0$ and $\xi_0 = 0$. The four parameters α_c , β_c , η_0 and ζ_0 are called the *cylinder extrinsic parameters*.

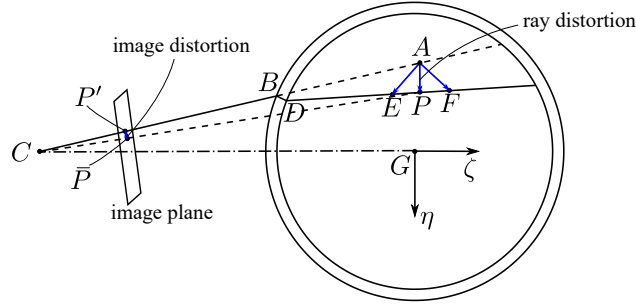


Figure 2: Definition of the cylindrical deformation. Distortion is exaggerated for clarity.

The cylinder geometry is identified uniquely by the internal radius r_i and the thickness Δr (when assuming an infinite height). These parameters, in addition to the extrinsic parameters, identify the 3D position and orientation of the internal and external surfaces of the cylindrical element, at which the refraction of the LOSs take place. The latter depends also on the ratio ρ of the refractive indexes of the two confining material media, according to the Snell's law: $\rho \sin \theta_i = \sin \theta_r$, with θ_i and θ_r the angles between the normal to the surface and the incident and the refracted ray, respectively. If the internal fluid is different from that outside of the cylinder, the ratio ρ assumes different values for the external and the internal surfaces of the cylinder sidewall; we denote such values with the symbols ρ_e and ρ_i , respectively. The four parameters r_i , Δr , ρ_e and ρ_i are the so-called *cylinder intrinsic parameters*.

The cylinder extrinsic and intrinsic parameters constitute the part of the model necessary to represent the cylindrical distortion; the remaining parameters are those of the pinhole camera model. The reader can find a throughout overview of the latter in the works by Tsai (1987) and Heikkila and Silven (1997).

The crucial point of the proposed innovative model is to determine the cylindrical distortion for a 3D point of the space inside the cylinder, once assigned the calibration (pinhole-camera and cylinder) parameters and assigned the coordinates of the point. Figure 2 schematically shows the distortion undergone by a LOS crossing the cylinder sidewall (solid black line). In Fig. 2, for simplicity, the ζ -axis has been assumed to be parallel to the line connecting the projection center C and the origin G of the cylinder reference frame. The figure shows that (neglecting lens distortions) the point P is imaged along the LOS $CBDEP$ and its image is the point P' . Without the cylinder, P would be imaged along the line PC and its image would be the point \bar{P} , while the LOS corresponding to the point P' would be the straight line AC . The image distortion caused by the cylinder is given by the vector $P' - \bar{P}$. Once computed such a distortion, the image point P' can be obtained simply by adding it to the vector position of the point \bar{P} , which is in turn determined by applying the classical pinhole camera model (Tsai, 1987; Heikkila and Silven, 1997).

It is now noted that the determination of the image distortion $P' - \bar{P}$ is possible only in an implicit way. In fact, given the image point P' , the LOS AC is identified and it is immediate to determine the distorted LOS $PEDBC$ by using Snell's law. Conversely, given the object point P , the LOS $PEDBC$ is not immediately identified. In this case, the problem is finding among the infinite rays that start from P the one that reaches the projection center C . Obviously, by virtue of the principle of the optical reciprocity, this is equivalent to find among the infinite rays that start from C the one that reaches the object point P . In the present implementation of the model, the above problem is addressed in the latter way.

By focusing on the LOS AC in Fig. 2, it is possible to define a ray distortion as the distance of the point A from the distorted LOS $PEDBC$. If the easiest way to measure this distance is in the plane normal to one of the two LOSs, in principle it is possible to measure it in any plane except that parallel to the distorted LOS. For instance, the vectors $E - A$, $P - A$ and $F - A$ are all representative of the LOS deviation and can be assumed as ray distortion indifferently. In the present case, the ray distortion is evaluated in the plane passing through A and normal to the ζ -axis; therefore, it is coincident with the vector $P - A$ in Fig. 2. Such a distortion is denoted with the symbol $\delta_c P$.

Therefore, given the point A , it is possible to determine the distorted LOS $PEDBC$ similarly to the case when the image point P' is assigned, calculate the ray distortion $\delta_c P$ and then the "distorted" position P as:

$$P = A + \delta_c P(A). \quad (2)$$

Vice versa, given the object point P , an iterative procedure has to be applied to determine the position A from equation (2). In particular, a Newton-Raphson method starting from the initial guess $A = P$, which cor-

responds to the case of zero distortion, is used in the present implementation of the model. Once determined A , the image point P' is readily obtained by applying the classical pinhole camera model.

In short, the above described model is based on straightening the LOSs of the points imaged through the cylinder. This is done by subtracting the cylindrical ray distortion from the position of the object points and subsequently applying the perspective projection transformation. The determination of the ray distortion is performed in the cylinder reference frame: in such a way it is possible to reduce the computational burden since both the intersections line/cylindrical surface and the application of Snell's law are cheaper when the cylinder axis coincides with one of the coordinate directions.

Although the above treatment has focused on the projection of points inside the cylinder, the present model can be applied to map the whole region surrounding the cylinder sidewall. In fact, the points that are not imaged through the cylinder are characterized by a zero ray distortion ($\delta_c P(A) = 0$) and therefore consistent with the model, whereas for the points behind the cylinder, the ray distortion can be computed by determining the deviation of the LOSs through the sidewall both when entering and when exiting the cylinder. In principle, also the points falling inside the sidewall can be mapped by the model. Nevertheless, it should be noted that some LOSs intersecting the external surface undergo total internal reflection and following their path may become very complicate. In such a case, the ray distortion is assigned a value equal to zero. Although this results in the projection of a point that is not actually visible, it does not represent a problem since the interior of the sidewall is generally not imaged. On the other side, imaging of the points behind the cylinder is used in the calibration of the camera system as explained in the next section.

3 Calibration procedure

The camera calibration based on the pinhole camera model with the refraction correction for imaging through a cylinder consists essentially of two steps: identification of the pinhole-camera parameters and identification of the cylinder parameters. If possible, it is convenient to perform these two steps separately in order to facilitate the convergence of the optimization algorithms used for the parameter estimation.

The pinhole-camera parameters can be determined via a classical target-based calibration in absence of the cylinder, as shown in Figure 3a. As a further step, when possible, a volume self-calibration (Wieneke, 2008; Discetti and Astarita, 2014; Wieneke, 2018) can be performed still in absence of the cylinder, thus improving the accuracy in the estimation of the pinhole-camera parameter. Subsequently, the cylinder parameters can be identified by placing the cylinder in situ and recording and analyzing the images of the calibration target distorted by its sidewall. This is done in principle by inserting the calibration plate inside the cylinder, placing it in several known positions within the cylinder inner volume. When it is not possible to operate in such a way (i.e., the cylinder interior is not accessible), the calibration target can be placed in a known position behind the cylinder, at a small distance from the sidewall in such a way that a sufficient number of markers is in focus in that position (see Fig. 3b). The cylinder parameters are determined via nonlinear least-squares optimization starting from the known 3D world position of the markers and their 2D locations detected in the distorted image. When more than one camera is used, this optimization is performed in a combined way for all the cameras of the imaging system and thus a unique set of optimal cylinder parameters is found, keeping the pinhole-camera parameters determined in the first stage of the procedure unchanged.

The initial values of the cylinder parameters are easily assigned when the geometrical and physical properties ($r_i, \Delta_r, \rho_i, \rho_e$) of the cylinder are known (or measured) and the relative location and orientation of the world reference frame with respect to the cylinder reference frame are correctly estimated. Obviously, the best practice is to choose a world reference frame such that the extrinsic cylinder parameters ($\alpha_c, \beta_c, \eta_0, \zeta_0$) are small, in such a way that their initial values can be set to zero.

The last step of the calibration procedure consists in a volume self-calibration (Fig. 3c), where all the parameters of the model, both the pinhole-camera ones and the cylinder ones, are optimized at the same time.

It is worth noting that the above procedure is effective when it is possible to place the cylinder in situ after the calibration of the pinhole-camera parameters. Otherwise, the estimation of the calibration parameters can be considerably hard, since the non-linearity of the model implies, as above explained, iteration and the convergence of the employed iterative methods strongly depends on the initial guess values. While the cylinder parameters can be easily estimated, some of the pinhole camera parameters might be more difficult to evaluate. In the latter case, we still suggest to separate the identification of the pinhole-camera model from that of the cylinder parameters. The cylinder interior has to be swept by a calibration plate, which should be designed appropriately to cover regions as close as possible to the cylinder sidewall. As a first step, the

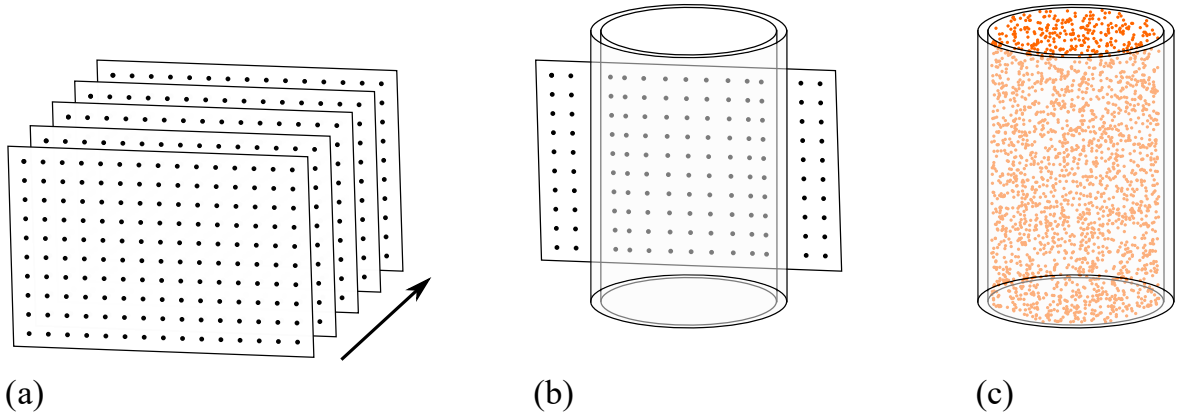


Figure 3: Camera calibration procedure: (a) identification of the pinhole-camera parameters via target-based calibration; (b) identification of the cylinder parameters; (c) volume self-calibration.

pinhole-camera parameters can be estimated by using the control points affected by the smallest cylindrical ray distortions. For this purpose, it is possible to neglect the cylindrical distortion and use the direct linear transformation (DLT) (Heikkila and Silven, 1997) for estimation of the perspective projection parameters and then determine the lens distortion parameters (of the full pinhole-camera model) by means of non-linear optimization methods. This procedure is carried out separately for each camera and provides a fairly good estimation of the pinhole-camera parameters to be used as initial values for the calibration of the complete model. The next step indeed consists in optimizing both the pinhole-camera parameters and the cylinder ones using all the control points available. Finally, a further refinement of the calibration parameters can be obtained via volume self-calibration.

4 Results and discussion

In this section, the proposed camera calibration model is comparatively assessed against the classical pinhole camera model and the polynomial models, based on the experimental measurements of Rayleigh-Bnard convection inside a cylinder with aspect ratio equal to $1/2$.

The sample cylinder is made of Plexiglas and immersed in a tank filled with water at a temperature of 17.5°C . As a consequence, the refractive index ratio at the external side of the cylinder wall is $\rho_e = 0.89$, while at the internal side $\rho_i = 1/\rho_e = 1.12$. The internal radius is $r_i = 74$ mm and the wall thickness is $\Delta r = 3$ mm. Thermal convection is maintained inside the cylinder by heating the bottom and cooling the top with a constant temperature difference of 5°C (resulting in a Rayleigh and a Prandtl number of about 1.86×10^8 and 7.6, respectively). Complete information about the experimental apparatus is given in Paolillo et al. (2018).

The T-PIV system is made of a dual pulse Nd:YAG and four Andor sCMOS cameras, arranged in a planar configuration with an angular spacing of 40° and equipped with 28 mm focal length objectives (the resulting digital resolution is about 14 voxel/mm). The laser light is shaped into a cylindrical beam that illuminates the whole cell interior by crossing the transparent heat exchanger on its top.

4.1 Assessment of the proposed camera model

The distributions of the self-calibration residual disparities of the classical pinhole camera model and the novel proposed model are comparatively shown in Fig. 4 for one of the four cameras employed. An identical self-calibration process has been carried out in both cases, setting the same process parameters and starting from the pinhole-camera parameters obtained by a target-based calibration performed without the cylinder in situ. It is immediate to note that the histogram related to the classical pinhole camera model (blue) exhibits a broader distribution with fairly high values of the relative frequency of occurrence up to 0.64 pixels. From the error scatter plot in the top right part of Fig. 4, it is also clear that the greatest component of the disparity errors is that in the Y -direction, which is roughly normal to the cylinder axis, as reasonably expected.

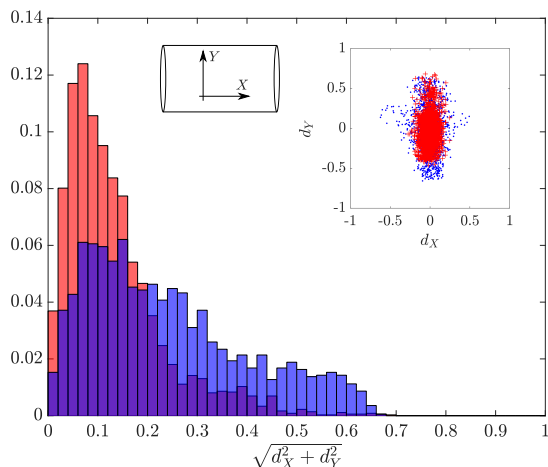


Figure 4: Experimental assessment of the proposed camera model against the classical pinhole camera model. Normalized histograms and scatter plots of the calibration residual errors (in pixel units). Blue markers correspond to the classical pinhole camera model, red ones to the novel model.

Although the superiority of the proposed model is already evident from the above observations, Fig. 4 does not provide a full picture of the comparative assessment, leading to an overestimation of the performance of the classical pinhole camera model. This is essentially due to the fact that in the self-calibration procedure it is not possible to assign a disparity vector to sub-volumes where the triangulation errors are too large and cause the formation of a high number of ghost particles with a subsequent considerable dispersion in the disparity map. In an attempt to take account of this shortcoming, Fig. 5 reports a scatter plot of the average position of all the triangulated particles (both true and ghost) in the sub-volumes where a disparity peak is detected with sufficient S/N ratio (greater than 2) for both the examined camera models. The figure shows that the regions adjacent to the cylinder sidewall at large y locations are affected by the greatest triangulation errors; in particular, these errors are expected to be greater than the search radius used in the triangulation procedure itself, which is equal to 2 pixels for the considered case.

As concerns the comparison between the proposed model and the polynomial models, it should be remarked that a direct comparison is not possible in the present experiments due to inaccessibility of the cylinder volume, which makes calibration of the polynomial model infeasible. On the contrary, in the following, the pinhole camera model with the refraction correction for the cylindrical distortion is assumed as a reference and a virtual calibration of the polynomial models is performed starting from pairs of arbitrarily chosen 3D world coordinates of points located inside the cylinder and the corresponding 2D image coordinates given by the calibrated reference model. The results of such virtual calibrations are reported in Fig. 6 in terms of the distribution of the calibration residual errors.

In Fig. 6a three different types of polynomial functions are compared: 3rd, 5th and 6th-order, respectively. It can be noted that the 3rd-order polynomial function leads to unacceptably high errors, while the other two models offers better performance, with the higher order polynomial having about the 75% of errors below 0.1 pixels. Figures 6b presents the distribution of the calibration errors for several multi-plane polynomial models using third-order in-plane polynomials and a different number of z -planes (2, 6 and 9, respectively). It should be noted that the 9-planes 3rd-order polynomial mapping function appears to behave worse than the 6th-order polynomial function of Fig. 6a. This might be ascribable to the piecewise linear interpolation along the z -direction underlying the multi-plane polynomial function, which could not be able to represent the cylindrical distortion in the regions adjacent to the sidewall with sufficient accuracy. Moreover, the analysis of the error scatter plots in Fig. 6a-b reveals that the error component in the Y -direction is considerably higher than that in the X -direction. Since these disparities are representative of the residual error of the polynomial functions in reproducing the mapping transformation of the pinhole camera model with the refraction correction, it is possible to conclude that polynomials are less effective in representing the image distortion in the direction normal to the cylinder axis than the proposed model.

Indeed, polynomials can offer performance comparable to that of the pinhole camera model with refraction correction only with a high order, which results in a large number of calibration parameters. In order to show that, we schematically report the main features of several camera models in Tab. 1. The table clearly

shows that the polynomial models that offer errors comparable to those of the pinhole camera model with refraction correction for the cylindrical distortion (polynomial with 6th order in x , y and z and the multi-plane polynomial with 5th order and 9 planes) are characterized by a number of calibration constants more than 6 times greater (168 and 378, respectively, against 25).

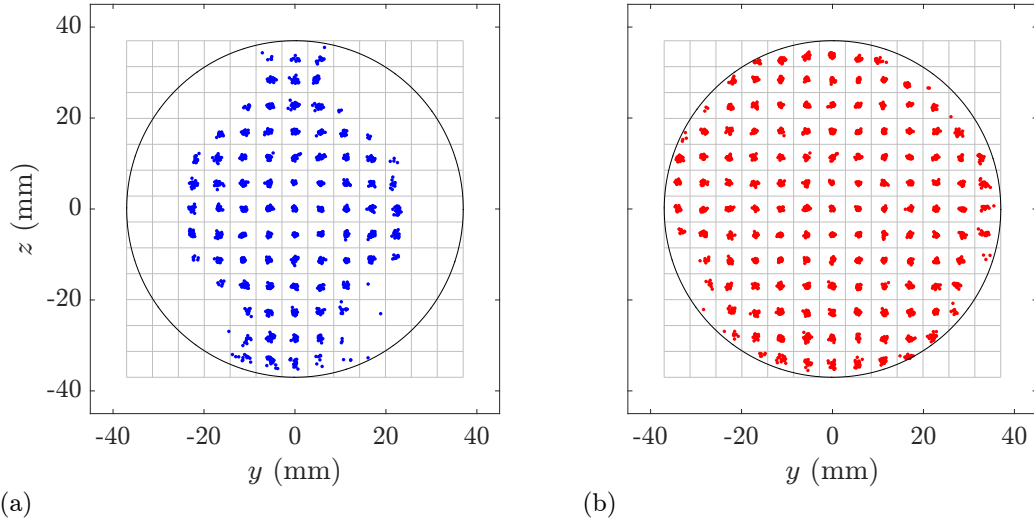


Figure 5: Volume self-calibration with (a) the classical pinhole camera model and (b) the model with refraction correction for the cylindrical deformation. Mean positions of the triangulated particles falling in separate sub-volumes of the whole illuminated volume. The sub-volumes are represented with solid gray lines.

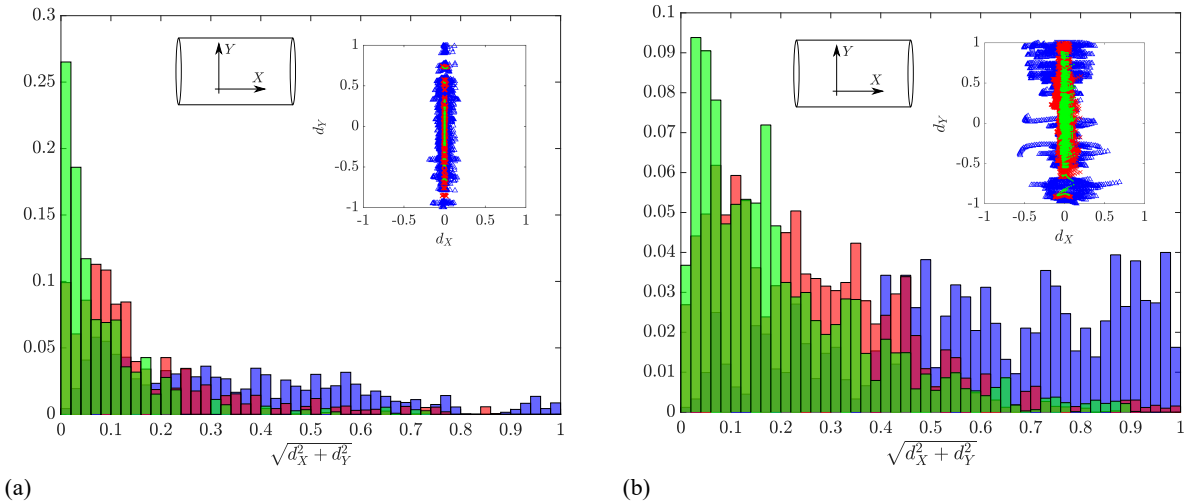


Figure 6: Experimental assessment of the novel pinhole-camera model with the refraction correction for the cylindrical deformation against the polynomial models. Normalized histograms and scatter plots of the calibration residual errors (in pixel units). Results of the virtual camera calibrations performed using: (a) polynomial mapping functions of order 3 (blue), 5 (red), 6 (green); (b) multi-plane polynomial models based on third-order polynomials on selected z -planes and piecewise linear interpolations along the z -direction; the numbers of z -planes employed are 2 (blue), 6 (red) and 9 (green).

Table 1: Main features of the investigated camera models. Results are related to the virtual calibrations performed starting from the calibrated pinhole camera model with the refraction correction. Results for the reference model are related to volume self-calibration. Errors are in pixel units.

model	# of par.	rms err.	median err.	99th percent.
pinhole with correction*	25	0.13	0.11	0.47
classical pinhole	17	1.42	1.06	6.37
polyn. $3 \times 3 \times 3$	40	0.53	0.36	3.72
polyn. $5 \times 5 \times 5$	112	0.18	0.10	1.05
polyn. $6 \times 6 \times 6$	168	0.085	0.047	0.65
2 z-planes polyn. $3 \times 3^\dagger$	40	3.48	3.27	10.27
6 z-planes polyn. $3 \times 3^\dagger$	120	0.29	0.23	1.34
9 z-planes polyn. $3 \times 3^\dagger$	180	0.23	0.16	1.19
2 z-planes polyn. $5 \times 5^\dagger$	84	3.46	3.30	10.54
6 z-planes polyn. $5 \times 5^\dagger$	252	0.19	0.15	0.76
9 z-planes polyn. $5 \times 5^\dagger$	378	0.097	0.07	0.44

*reference model

† piecewise linear interpolation along the z-direction

5 Experimental verification

Figure 7 shows the large-scale instantaneous velocity field of the thermal convection inside the cylinder. Time-resolved T-PIV measurements have been carried out at a frequency of 7.5 Hz and processed with an algorithm combining both methods based on algebraic tomographic reconstruction techniques and methods based on 4D particle tracking. More precisely, the process is started up by analyzing a first set of snapshots with the sequential-motion-tracking enhancement (SMTE) algorithm (Lynch and Scarano, 2015); therefore, tomographic reconstruction is based on multi-resolution iterations of the SMART and CSMART algorithms (Atkinson and Soria, 2009; Ceglia et al., 2014; Castrillo et al., 2016), while the velocity fields are obtained by multi-pass volumetric sparse cross-correlation as explained in Discetti and Astarita (2012a,b). In a second phase, time-resolved particle tracking is achieved via Shake-The-Box (STB) (Schanz et al., 2016) and iterative particle identification (Wieneke, 2012). This allows to considerably reduce the number of ghost particles and increase accuracy of measurements. At this stage, forward-time projection of particles is based on both extrapolation of known trajectories and cross-correlation. The final structured velocity fields are determined from particle velocities via a second-order polynomial interpolation method.

In Fig. 7 the isosurfaces of the vertical velocity component (parallel to the cylinder axis) are represented for the novel camera model, the classical pinhole camera model and the 3rd order polynomial camera model. In the former two cases, the optimal calibration parameters of the employed model have been determined via a self-calibration, whereas in the latter case a virtual calibration has been performed using the innovative model as reference, as explained in the previous section. However, the velocity fields related to different models have been obtained using the same process parameters for the motion analysis. It is interesting to note how in the case of the classical pinhole camera model measurements appear to be extremely noisy over the entire domain, although fairly good results might be expected at least in the central part (which is less affected by the cylindrical distortion). This can be explained by considering that, in principle the pinhole camera could work fine in the most inner part of the cylindrical sample, the optimal values of the calibration parameters determined with the self-calibration are those minimizing the (root) square sum of disparity errors over the whole measurement domain. However, from a global viewpoint, the velocity field structure is not significantly altered or lost in the vicinity of the sidewall. Much better results are instead observed in the case of the 3rd order polynomial function. Although not shown here for brevity, the time-averaged velocity field even on a short time interval exhibit minor difference between the three different examined cases. Conversely, greater discrepancies are found for the velocity fluctuations. In other words, the pinhole camera model and the polynomial models with low orders do not offer sufficient accuracy in the determination of the temporal statistics or time-derived quantities like fluid acceleration.

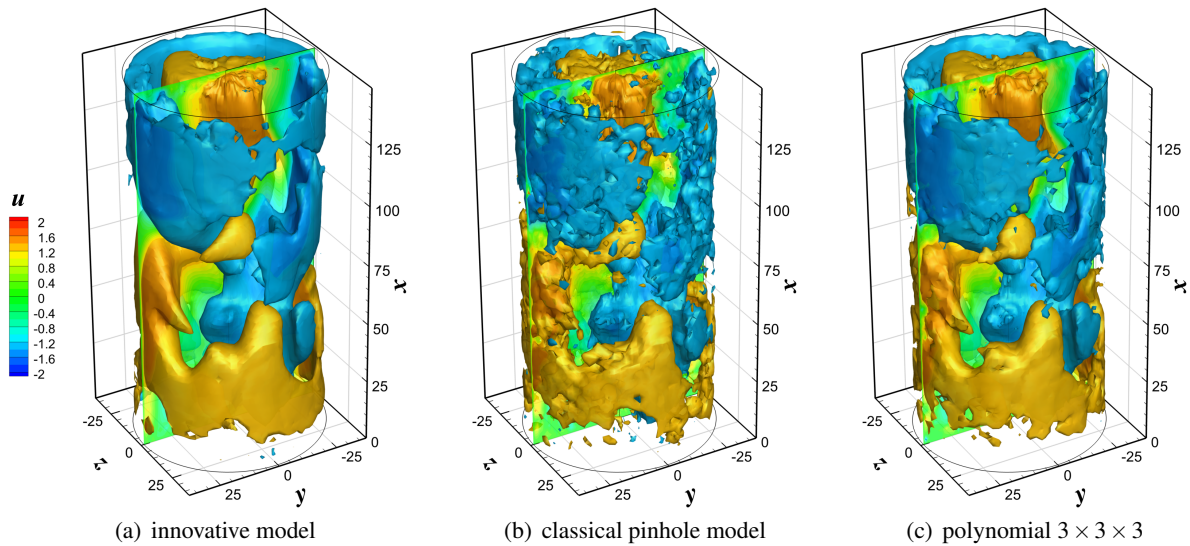


Figure 7: Comparison of different camera calibration models for velocity measurements of Rayleigh-Bénard convection inside a cylinder with aspect ratio equal to $1/2$ at Rayleigh and Prandtl numbers equal to 1.86×10^8 and 7.6 , respectively. Isosurfaces of the vertical velocity component (parallel to the cylinder axis). Velocity values are in mm/s, coordinates in mm.

6 Conclusions

The present work has introduced an innovative camera model to accurately represent the distortion caused by the curved sidewall of a transparent cylinder. The model consists essentially of an integration of the pinhole camera model with Snell's law of refraction; in this way, only a small number of parameters are added to the pinhole-camera ones: four extrinsic parameters, which identify the spatial position and orientation of the cylinder with respect to the world coordinate reference frame, and four intrinsic parameters, which define uniquely the geometry and optical properties of the sidewall.

A specific calibration procedure has been also detailed. Since the refraction correction for the cylindrical distortion has to be determined implicitly and the model also includes spherical lens corrections, non-linear least-squares optimization algorithms have to be used in the calibration process. To facilitate the convergence, the pinhole-camera parameters and the cylinder ones are optimized in separate steps. This is possible because all these parameters are independent from each other. An additional advantage of such a procedure is that there is no need of sweeping the entire measurement volume with a calibration target.

The proposed camera model has been comparatively assessed against other camera models by using experimental data from an investigation of Rayleigh-Bénard convection. While the classical pinhole-camera model has been found to be ineffective to map the cylinder interior especially in the regions adjacent to the sidewall, polynomial mapping functions can offer similar performance only with high orders, which however results in a very large number of parameters and occurrence of oscillations. When the degree of the polynomial is low, turbulent fluctuations and temporal statistics are not captured with sufficient accuracy.

References

- Agarwal AK, Gadekar S, and Singh AP (2017) In-cylinder air-flow characteristics of different intake port geometries using tomographic PIV. *Physics of Fluids* 29:095104
- Ahlers G, Grossmann S, and Lohse D (2009) Heat transfer and large scale dynamics in turbulent Rayleigh-Bénard convection. *Reviews of Modern Physics* 81:503–537
- Atkinson C and Soria J (2009) An efficient simultaneous reconstruction technique for tomographic particle image velocimetry. *Experiments in Fluids* 47:553

- Cafiero G, Ceglia G, Discetti S, Ianiro A, Astarita T, and Cardone G (2014) On the three-dimensional precessing jet flow past a sudden expansion. *Experiments in fluids* 55:1677
- Castrillo G, Cafiero G, Discetti S, and Astarita T (2016) Blob-enhanced reconstruction technique. *Measurement Science and Technology* 27:094011
- Ceglia G, Discetti S, Ianiro A, Michaelis D, Astarita T, and Cardone G (2014) Three-dimensional organization of the flow structure in a non-reactive model aero engine lean burn injection system. *Experimental Thermal and Fluid Science* 52:164–173
- Discetti S and Astarita T (2012a) A fast multi-resolution approach to tomographic PIV. *Experiments in Fluids* 52:765–777
- Discetti S and Astarita T (2012b) Fast 3D PIV with direct sparse cross-correlations. *Experiments in Fluids* 53:1437–1451
- Discetti S and Astarita T (2014) The detrimental effect of increasing the number of cameras on self-calibration for tomographic PIV. *Measurement Science and Technology* 25:084001
- Heikkila J and Silven O (1997) A four-step camera calibration procedure with implicit image correction. in *IEEE Computer Society Conference on Computer Vision and Pattern Recognition, San Juan, Puerto Rico, June 17-19*
- Lynch KP and Scarano F (2015) An efficient and accurate approach to MTE-MART for time-resolved tomographic PIV. *Experiments in Fluids* 56:66
- Marusic I, McKeon B, Monkewitz P, Nagib H, Smits A, and Sreenivasan K (2010) Wall-bounded turbulent flows at high Reynolds numbers: recent advances and key issues. *Physics of Fluids* 22:065103
- Paolillo G, Greco CS, Astarita T, and Cardone G (2018) Three-dimensional velocity measurements of Rayleigh-Bnard convection in a cylinder. in *Proceedings of 18th International Symposium on Flow Visualization*. Zurich, CH
- Scarano F (2012) Tomographic PIV: principles and practice. *Measurement Science and Technology* 24:012001
- Schanz D, Gesemann S, and Schröder A (2016) Shake-The-Box: Lagrangian particle tracking at high particle image densities. *Experiments in Fluids* 57:70
- Soloff SM, Adrian RJ, and Liu ZC (1997) Distortion compensation for generalized stereoscopic particle image velocimetry. *Measurement Science and Technology* 8:1441
- Tokgoz S, Elsinga GE, Delfos R, and Westerweel J (2012) Spatial resolution and dissipation rate estimation in Taylor–Couette flow for tomographic PIV. *Experiments in Fluids* 53:561–583
- Tsai R (1987) A versatile camera calibration technique for high-accuracy 3D machine vision metrology using off-the-shelf TV cameras and lenses. *IEEE Journal on Robotics and Automation* 3:323–344
- Wieneke B (2008) Volume self-calibration for 3D particle image velocimetry. *Experiments in Fluids* 45:549–556
- Wieneke B (2012) Iterative reconstruction of volumetric particle distribution. *Measurement Science and Technology* 24:024008
- Wieneke B (2018) Improvements for volume self-calibration. *Measurement Science and Technology* 29:084002